Electronic supplementary information (ESI)

TiO$_2$ superstructures with oriented nanospaces: A strategy for efficient and selective photocatalysis

Yuta Murakami, [a] Takashi Kamegawa, [b] Yasuhiro Kobori [ac] and Takashi Tachikawa *[ac]

[a] Department of Chemistry, Graduate School of Science, Kobe University, 1-1 Rokkodai-cho, Nada-ku, Kobe 657-8501, Japan

[b] Department of Applied Chemistry, Graduate school of engineering, Osaka Prefecture University, 1-2, Gakuen-cho, Naka-ku, Sakai, Osaka 599-8570, Japan

[c] Molecular Photoscience Research Center, Kobe University, 1-1 Rokkodai-cho, Nada-ku, Kobe 657-8501, Japan

*E-mail: tachikawa@port.kobe-u.ac.jp; TEL: +81-78-803-5736.

Table S1. Structural parameters of TMCs and reference samples

samples	surface area, $m^2\ g^{-1}$	mean pore size, nm	pore volume, $cm^3\ g^{-1}$	particle size, nm [a]
TMC-400	42	39	0.41	20
crushed TMC-400	28	51	0.35	20
TMC-800	13	24	0.076	29
P25	52	26	0.39	25

[a] Determined from the Scherrer's equation.
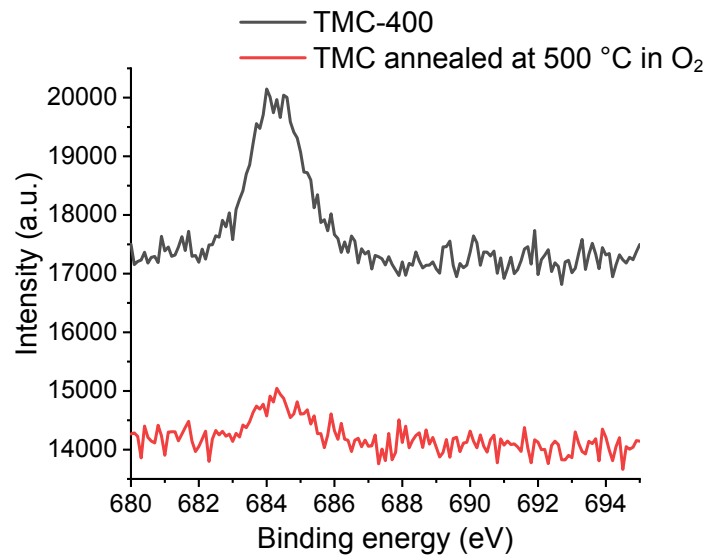
Fig. S1 F 1s XPS spectra of TMR-400 and TMR sintered at 500 °C for 8 h in oxygen atmosphere.
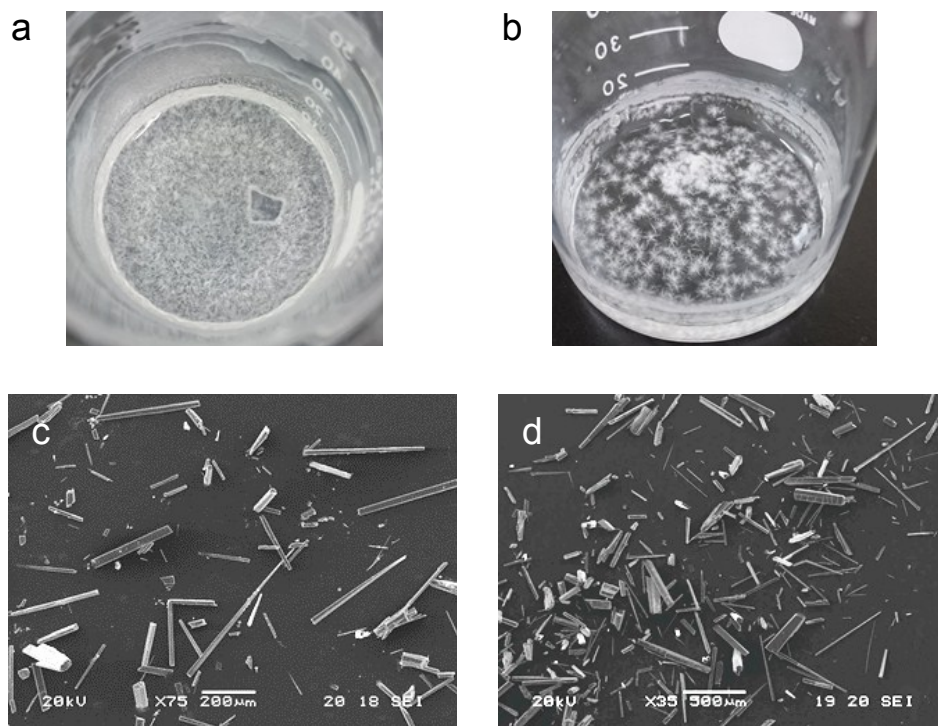

Fig. S2 (a,b) Optical and (c,d) SEM images of precursor crystals (a,c) with and (b,d) without a piece of silicon wafer.
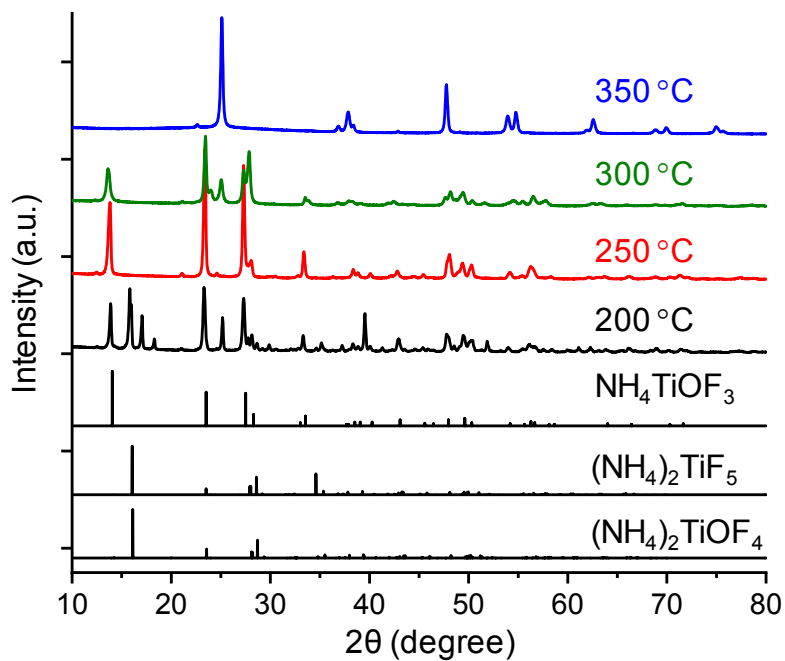
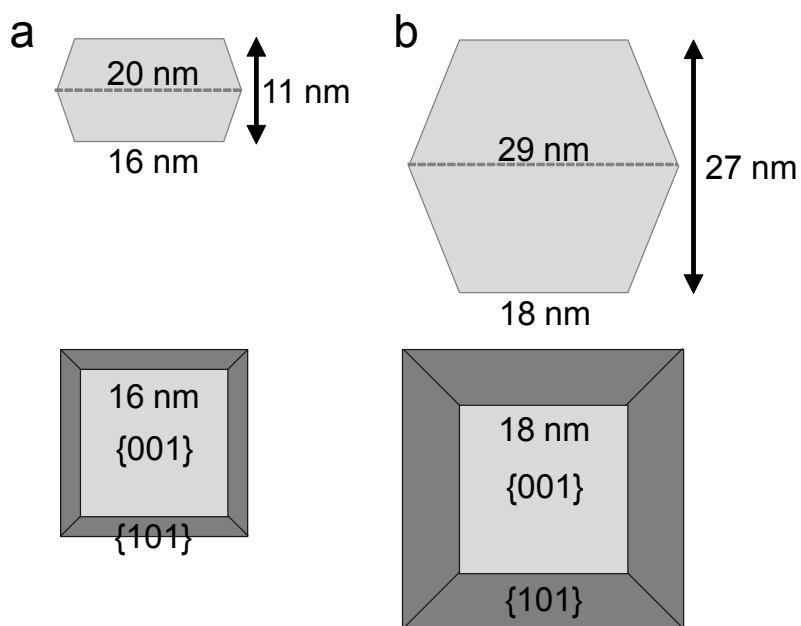**Fig. S3** Powder XRD patterns of the products obtained at different annealing temperature.

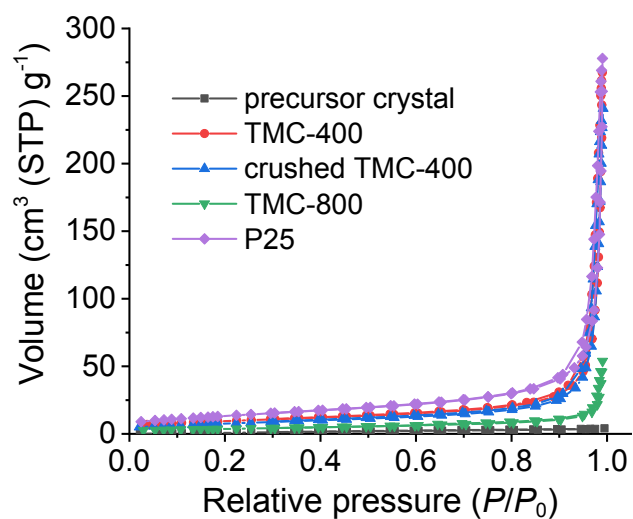**Fig. S4** Crystal shape and size of (a) TMC-400 and (b) TMC-800.

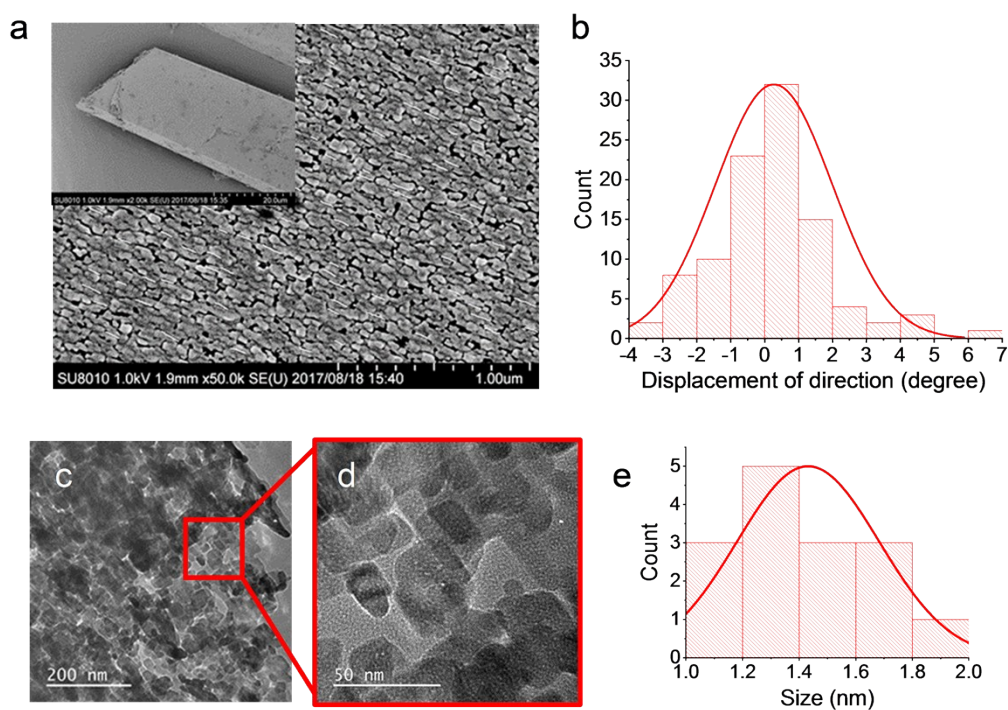**Fig. S5** N_2 adsorption-desorption isotherms of the materials.

Fig. S6 (a) FE-SEM images of the TMC-400 surface. (b) Direction displacement of the oriented nanospaces in the panel a. (c,d) TEM images of the oriented nanospaces. (e) Size distribution of the oriented nanospaces.
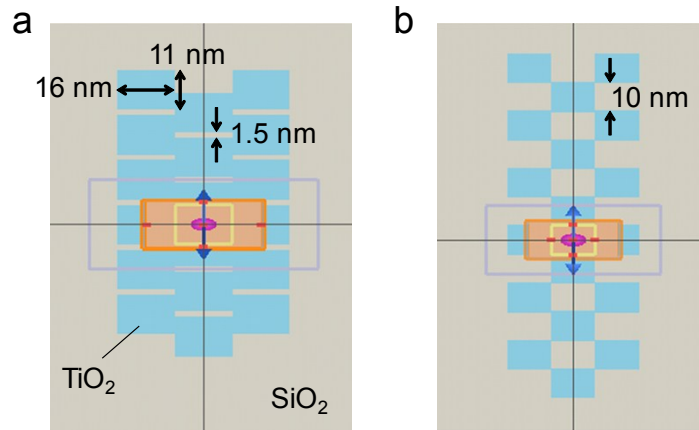
Fig. S7 (a) Structures used for FDTD calculations. The gaps between TiO_2 particles (16 nm (x) × 11 nm (y) × 16 nm (z)) on SiO_2 (1600 nm (x) × 1600 nm (y) × 1600 nm (z)) are set to 1.5 nm (a) and 10 nm (b). The orange and yellow squares indicate the simulated and monitored regions, respectively. The purple and blue arrows represent the incident direction of light and its polarization direction, respectively.
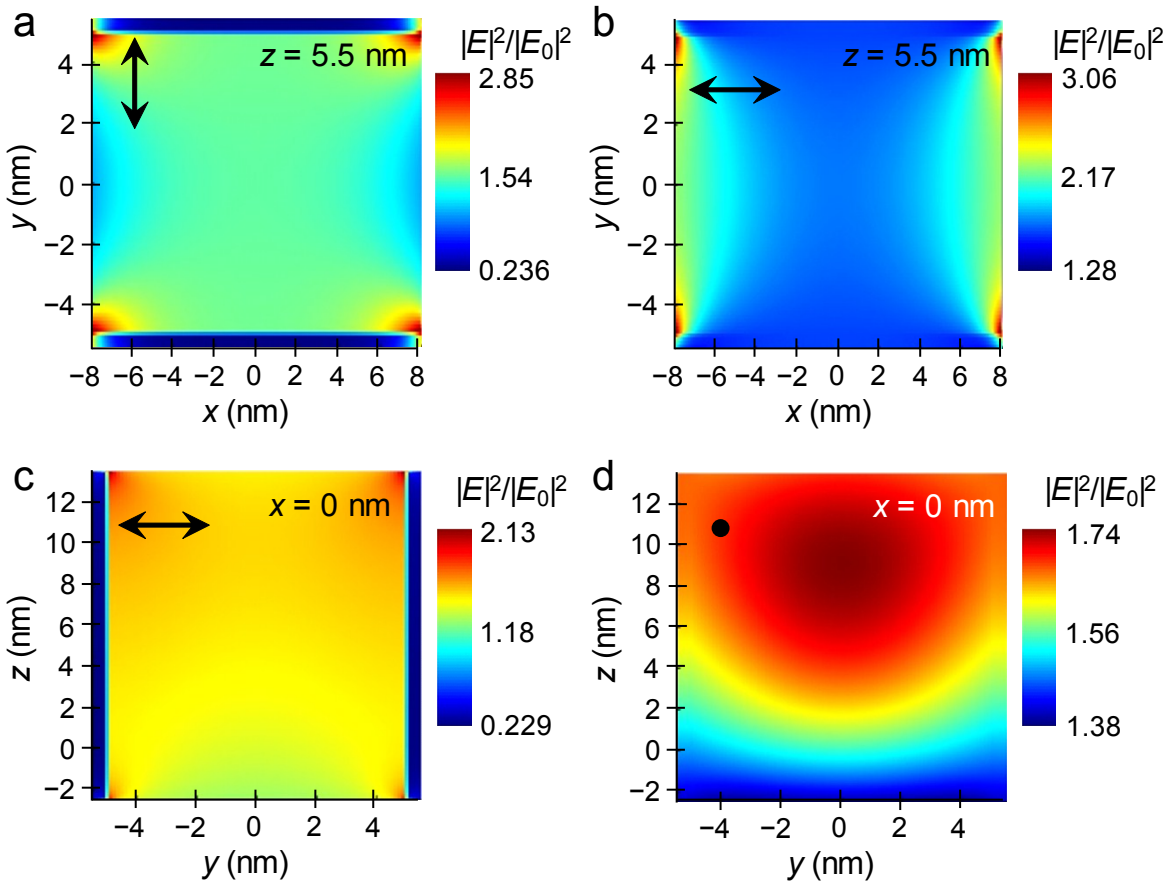
Fig. S8 (a,b) Distributions of electric fields obtained from the FDTD calculations in the gap of 10 nm between two rectangular TiO_2 particles at the x–y plane cut at the center of TiO_2 particle (z = 5.5 nm) when the polarization of the incident light (λ = 405 nm) is along y (a) and x (b) axes. (c,d) Distributions of electric fields at the y–z plane cut at the center of TiO_2 particle (x = 0 nm) when the polarization of the incident light is along y (c) and x (d) axes. The arrows in images represent the polarization direction of incident light.
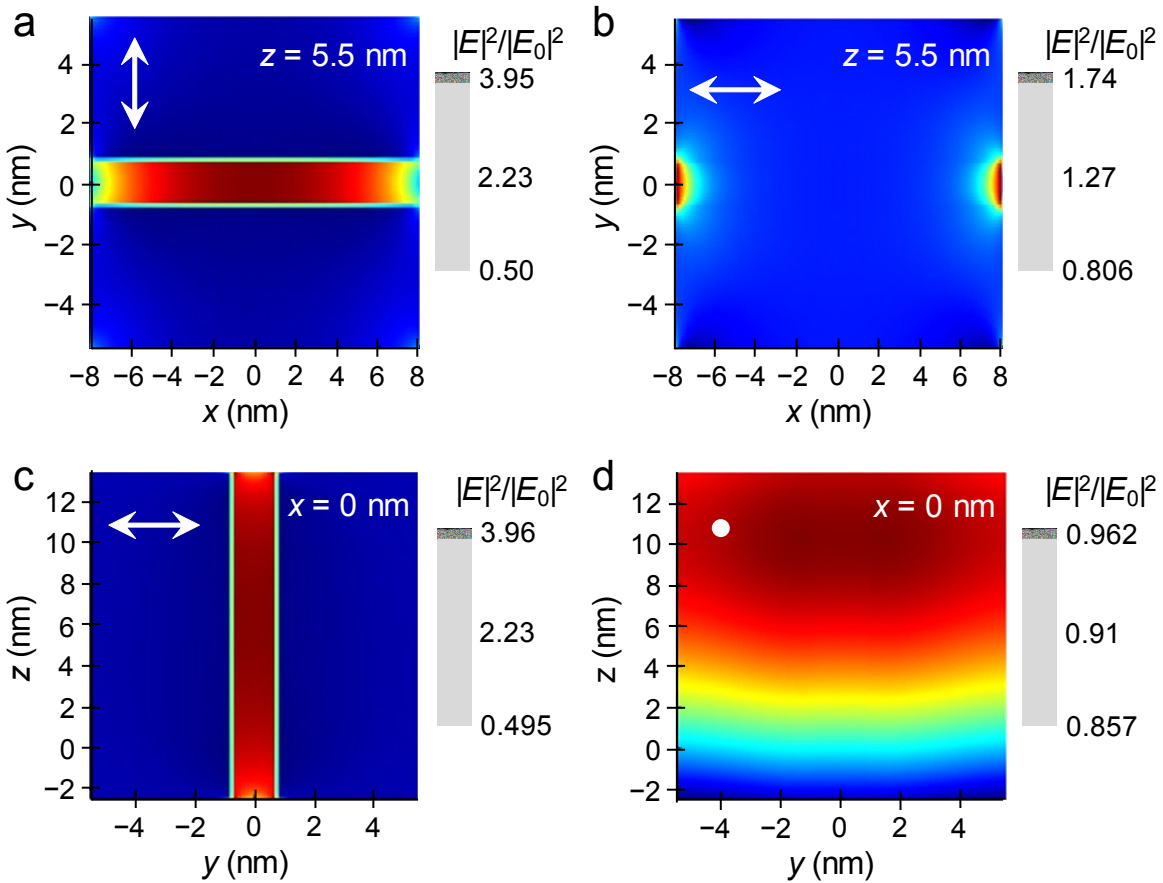
Fig. S9 (a,b) Distributions of electric fields obtained from the FDTD calculations in the gap of 1.5 nm between two rectangular TiO_2 particles at the x–y plane cut at the center of TiO_2 particle ($z = 5.5$ nm) when the polarization of the incident light ($\lambda = 365$ nm) is along y (a) and x (b) axes. (c,d) Distributions of electric fields at the y–z plane cut at the center of TiO_2 particle ($x = 0$ nm) when the polarization of the incident light is along y (c) and x (d) axes. The arrows in images represent the polarization direction of incident light.
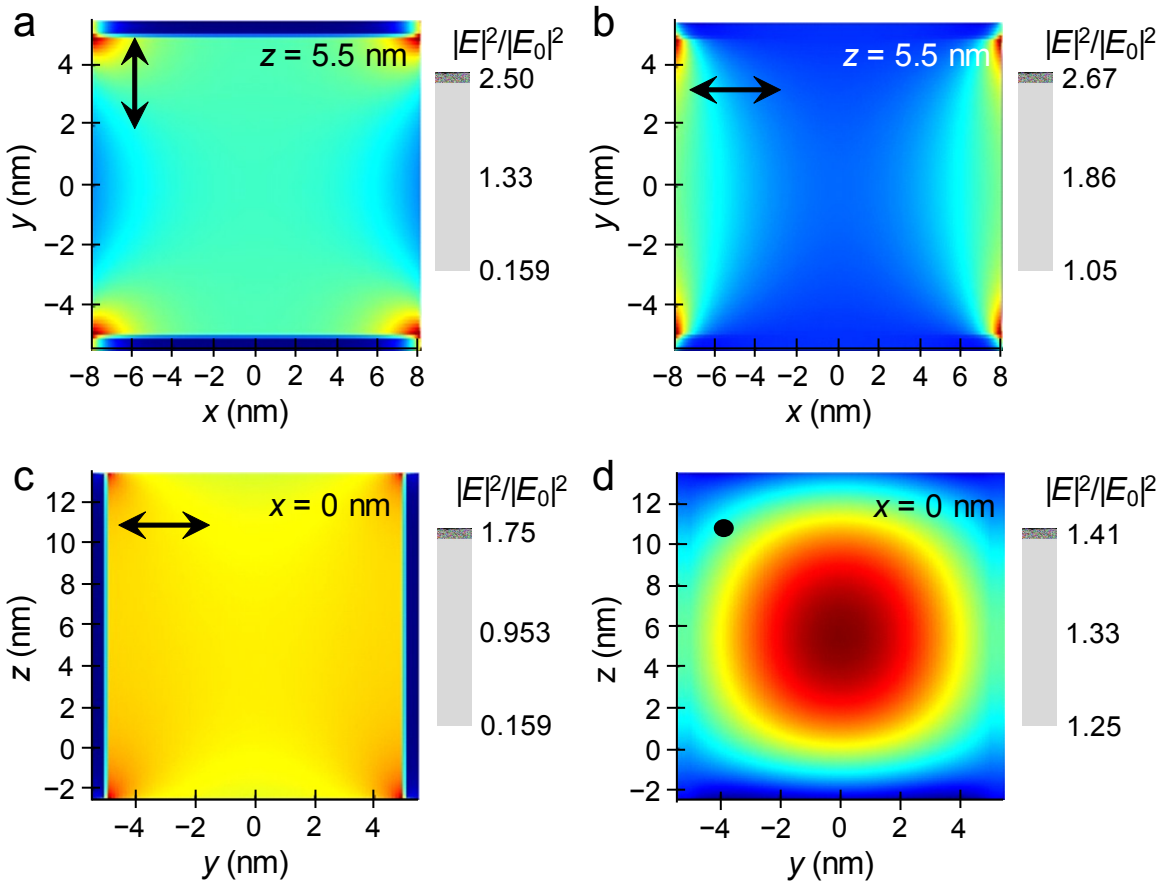
Fig. S10 (a,b) Distributions of electric fields obtained from the FDTD calculations in the gap of 10 nm between two rectangular TiO$_2$ particles at the x–y plane cut at the center of TiO$_2$ particle (z = 5.5 nm) when the polarization of the incident light (λ = 365 nm) is along y (a) and x (b) axes. (c,d) Distributions of electric fields at the y–z plane cut at the center of TiO$_2$ particle (x = 0 nm) when the polarization of the incident light is along y (c) and x (d) axes. The arrows in images represent the polarization direction of incident light.
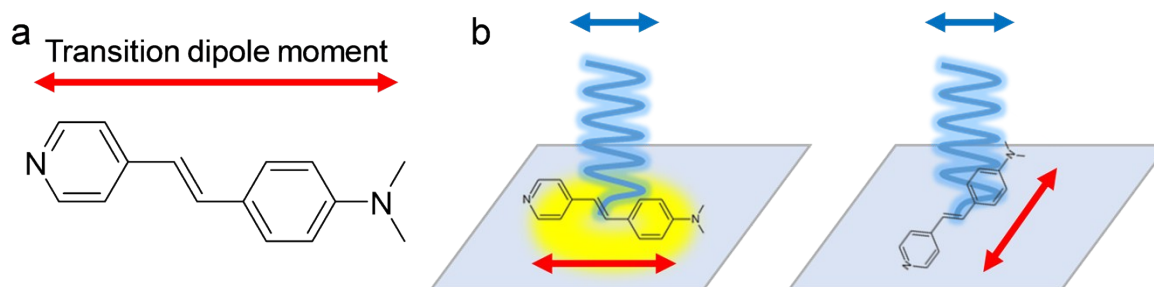
Fig. S11 (a) The molecular structure and transition dipole moment of 4-[4-(dimethylamino)-styryl]pyridine (DMASP). (b) Polarization-dependent fluorescence of DMASP. When the polarization of the excitation light is parallel (or perpendicular) to a transition dipole moment of DMASP, fluorescence becomes the maximum (or minimum).
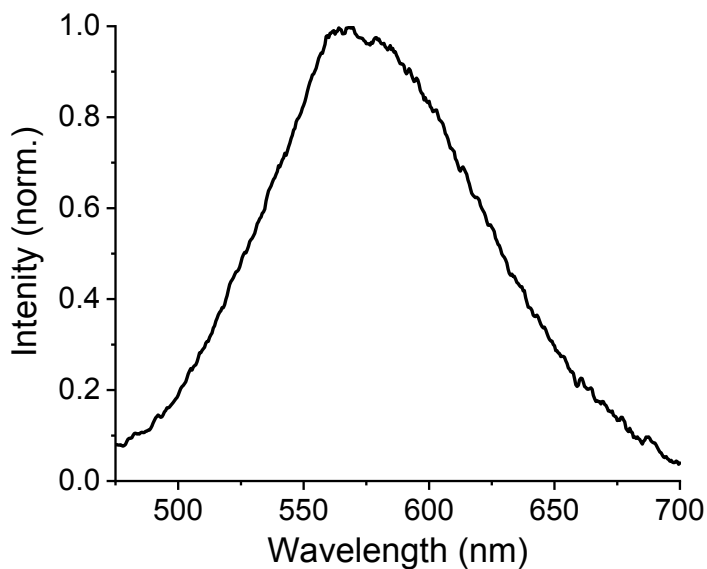

Fig. S12 Fluorescence spectrum of DMASP-adsorbed TMC in ambient air under 405-nm laser excitation.
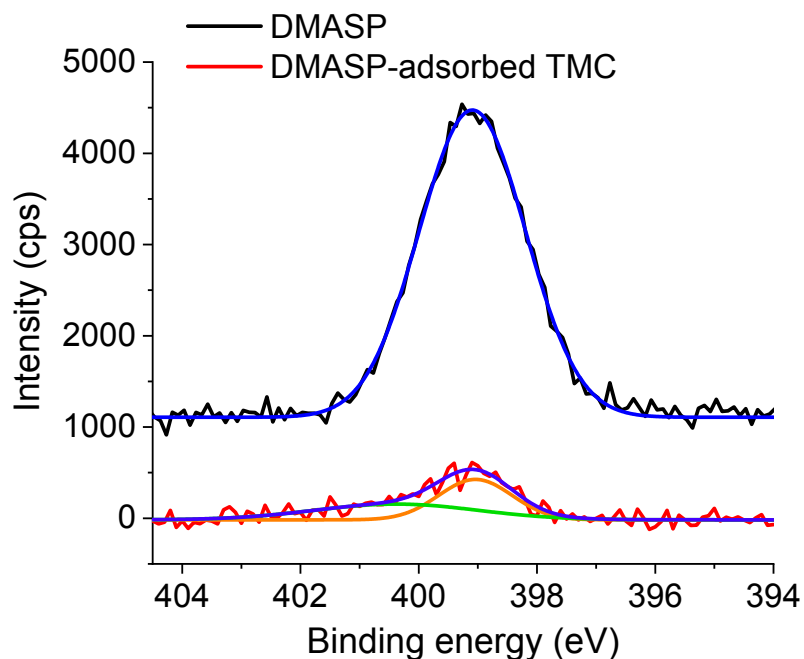
Fig. S13 N 1s XPS spectra of DMASP adsorbed on TMC (black) and amorphous DMASP molecule (red). The blue lines are the Gaussian fits. The 2 eV shift in the peak position toward a higher binding energy was observed for DMASP-adsorbed TMC (orange and green lines).
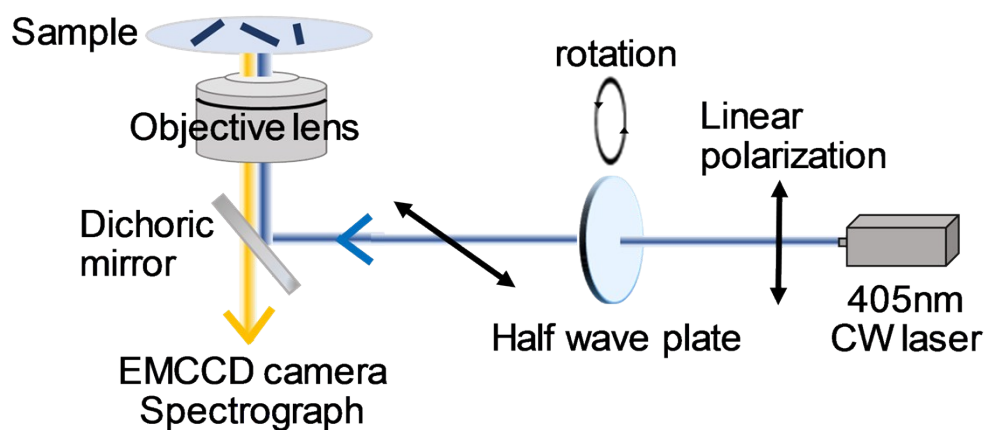

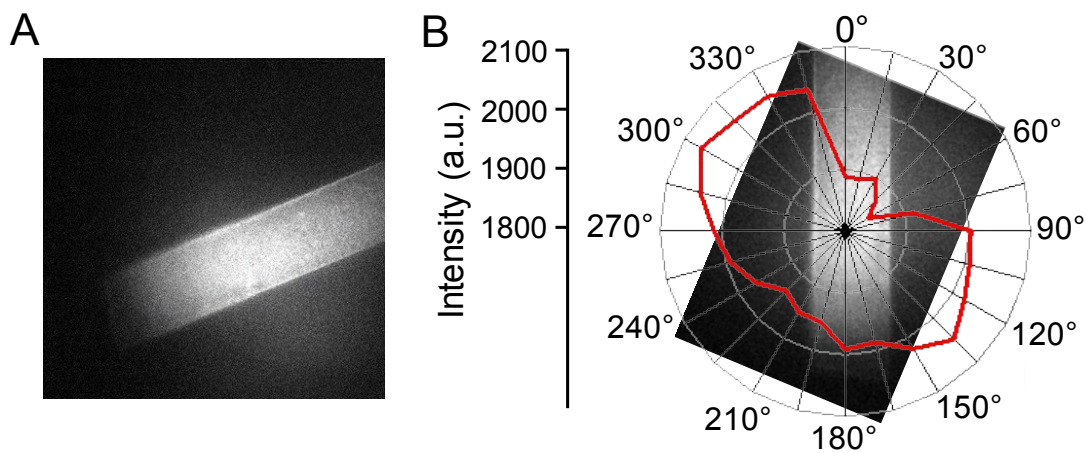**Fig. S14** Illustration of fluorescence microscope system.

Fig. S15 (a) A fluorescence image of DMASP-adsorbed TMC-800. The long and short axes of TMC are defined as 0° and 90°, respectively. (b) Azimuthal plot of the fluorescence intensity response of the DMASP to the polarization of excitation light. The percentage difference was calculated to be $8 \pm 3\%$.
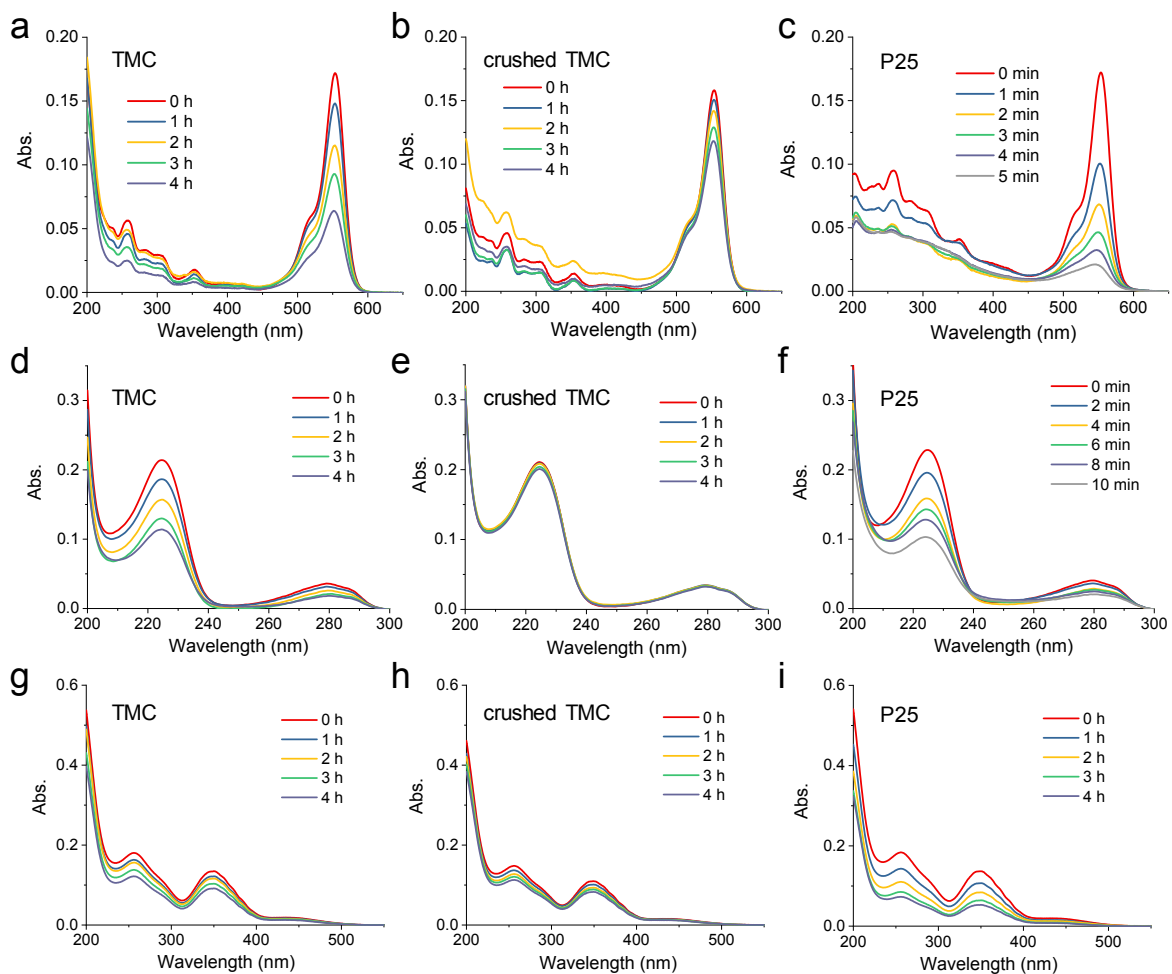
Fig. S16 UV-vis absorption spectra of the test solutions containing (a-c) RhB, (d-f) 4-CP, or (g-i) Cr^{6+} before and after UV irradiation.
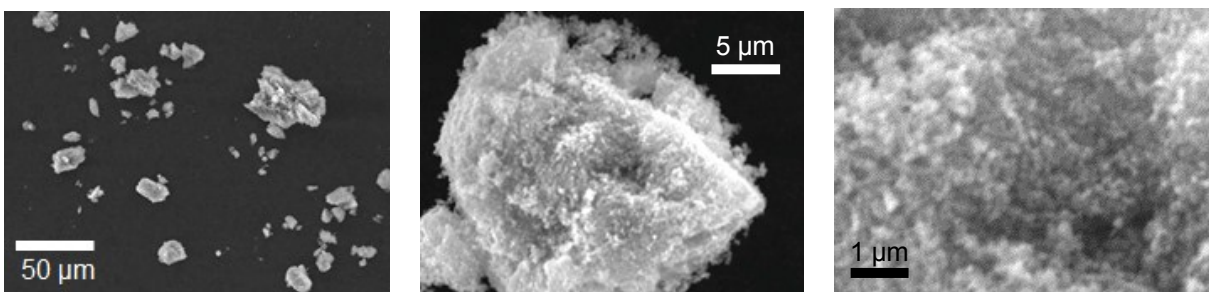

Fig. S17 SEM images of crushed TMC.